Research Article

Composition-dependent structural characteristics and mechanical properties of amorphous SiBCN ceramics by *ab-initio* calculations

Yuchen Liu[a,b], Yu Zhou[a], Dechang Jia[a,*], Zhihua Yang[a], Wenjiu Duan[c,*],
Daxin Li[a], Shuzhou Li[d], Ralf Riedel[e], Bin Liu[b,*]

[a]*Institute for Advanced Ceramics*, *School of Materials Science and Engineering*,
Harbin Institute of Technology, *Harbin 150001*, *China*
[b]*School of Materials Science and Engineering*, *Shanghai University*, *Shanghai 200444*, *China*
[c]*Tsinghua Shenzhen International Graduate School*, *Tsinghua University*, *Shenzhen 518055*, *China*
[d]*School of Materials Science and Engineering*, *Nanyang Technological University*, *Singapore 639798*, *Singapore*
[e]*Institut für Materialwissenschaft*, *Technische Universität Darmstadt*, *Darmstadt D-64287*, *Germany*

Abstract: The atomic structural features and the mechanical properties of amorphous silicoboron carbonitride ceramics with 13 different compositions in the Si–BN–C phase diagram are investigated employing *ab-initio* calculations. Both chemical bonds and local structures within the amorphous network relate to the elemental composition. The distribution of nine types of chemical bonds is composition-dependent, where the B–C, Si–N, Si–C, and B–N bonds hold a large proportion for all compositions. Si prefers to be tetrahedrally coordinated, while B and N prefer sp^2-like trigonal coordination. In the case of C, the tetrahedral coordination is predominant at relatively low C contents, while the trigonal coordination is found to be the main feature with the increasing C content. Such local structural characteristics greatly influence the mechanical properties of SiBCN ceramics. Among the studied amorphous ceramics, $SiB_2C_3N_2$ and $SiB_3C_2N_3$ with low Si contents and moderate C and/or BN contents have high elastic moduli, high tensile/shear strengths, and good debonding capability. The increment of Si, C, and BN contents on this basis results in the decrease of mechanical properties. The increasing Si content leads to the increment of Si-contained bonds that reduce the bond strength of SiBCN ceramics, while the latter two cases are attributed to the raise of sp^2-like trigonal configuration of C and BN. These discoveries are expected to guide the composition-tailored optimization of SiBCN ceramics.

Keywords: ultra-high-temperature ceramics; density functional theory (DFT); amorphous structure; mechanical properties

* Corresponding authors.

E-mail: D. Jia, dcjia@hit.edu.cn;

    W. Duan, dwenjiu@foxmail.com;

    B. Liu, binliu@shu.edu.cn

1 Introduction

Nitrides and carbides of silicon and boron own high kinetic and thermodynamic stability as well as thermomechanical durability originating from their predominantly covalent bonding constituents. These non-oxide ceramics have been proven to be the primary choice for high-temperature applications including propulsion systems and components in aerospace vehicles [1,2]. Among them, the quaternary amorphous SiBCN ceramics with low density, high hardness, good wear resistance, high-temperature stability up to 2000 ℃, and oxidation resistance up to 1600 ℃ emerge ahead of the classical non-oxide ceramics, namely Si_3N_4 and SiC [3–5]. The former is under the risk of decomposition at about 1400 ℃ in vacuum and 1775 ℃ in 0.1 MPa nitrogen, while the latter faces the high ablation rate due to the serious active oxidation at temperatures beyond 1500 ℃ [6]. Thus, continuous interest has led to active and intensive efforts on engineering their physical and chemical properties [7,8].

The quaternary SiBCN system provides composition variety, which enables their property optimization in various directions. For example, increasing the N content in SiBCN ceramics results in an increase of the electrical resistivity and the optical gap [9]. The excellent electromagnetic wave absorption capability can be obtained by adjusting the B content of SiBCN ceramics [10]. The incorporation of early transition metals into SiBCN ceramics leads to the enhancement of segregation tendency [11]. Until now, as the complicated nonequilibrium high-temperature reactions during synthesizing processes lead to multiphase compositions and microstructures [12–14], the characterization of intrinsic structures and properties of amorphous SiBCN materials is still challenging. It can only be achieved on the basis of fundamental studies related to the amorphous network structure of SiBCN. More detailed researches are required for the reliable prediction and understanding of the composition-dependent performance of these amorphous materials. However, this dependence is still not well understood from an experimental point of view, partly due to a lack of methodologies and facilities. Meanwhile, the high cost and time consumption make it an impossible mission to develop the design guidelines for the quaternary composition designing guidelines from independent experiments.

From a theoretical point of view, the most concerned issue of SiBCN materials is to deduce the regularity of the composition-dependent structure characteristics and the concomitantly influenced properties. The *ab-initio* calculations that provide reliable atomic scale information in an efficient manner have been demonstrated to be a powerful tool to investigate amorphous materials, including amorphous carbon [15], amorphous silicon [16], metallic glass [17], and amorphous ternary and quaternary ceramics in the Si–B–C–N system [18–20]. For the concerned amorphous SiBCN ceramics, efforts have been made to study the effect of the constituting elements (like boron [21] or nitrogen [9,22]) and/or the ratio variation of elements (like C/Si ratio [23] and B/(Si+B+C) ratio [24]) on their structure and physical properties. Although these works have provided some information, there is still a lack in concluding the underlying relationships among elemental compositions, bonding types, and properties. This lack of understanding is due to the limited knowledge on how the type of chemical bonds and the individual atomic coordination are influenced by the variation of the SiBCN composition.

A sequence of amorphous SiBCN ceramics with different compositions are modeled and studied in this work. In experiments, graphite, silicon, and boron nitride are generally used as the raw materials to fabricate SiBCN ceramics [4]. Correspondingly, a pseudo-ternary phase diagram with these three compounds as the corners is constructed. In this diagram, 13 compositions are selected by tuning their quaternary elemental compositions, which is implemented to avoid unrealistically atomic overlaps. Details of these SiBCN ceramics are shown in Fig. 1 and Table 1. The
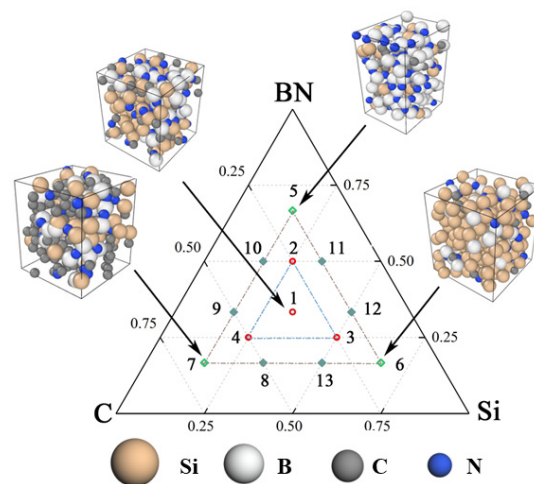

Fig. 1 Pseudo-ternary composition diagram for SiBCN ceramics.

Table 1 Atomic compositions, atomic numbers in supercells, calculated densities, and average atomic displacements during liquid mixing (Stage 1) and quenching (Stage 2) procedures for the studied compounds

	Composition	Atomic number in supercell	Calculated density (g/cm³)	Atomic composition				Average atomic displacement (Å)	
				Si	B	C	N	Stage 1	Stage 2
1	SiBCN	252	2.65	1/4	1/4	1/4	1/4	7.5±3.3	7.2±3.0
2	SiB_2CN_2	252	2.56	1/6	1/3	1/6	1/3	8.0±3.4	6.9±3.1
3	Si_2BCN	270	2.63	2/5	1/5	1/5	1/5	9.1±4.4	8.4±3.6
4	$SiBC_2N$	270	2.63	1/5	1/5	2/5	1/5	8.4±3.8	7.4±3.8
5	SiB_4CN_4	270	2.55	1/10	2/5	1/10	2/5	8.1±3.6	7.0±3.6
6	Si_4BCN	252	2.67	4/7	1/7	1/7	1/7	9.0±4.1	8.3±3.6
7	$SiBC_4N$	252	2.57	1/7	1/7	4/7	1/7	7.8±3.6	7.0±3.1
8	Si_2BC_3N	252	2.63	2/7	1/7	3/7	1/7	8.5±3.7	7.8±3.3
9	$SiB_2C_3N_2$	288	2.63	1/8	1/4	3/8	1/4	7.6±3.2	7.0±3.2
10	$SiB_3C_2N_3$	270	2.53	1/9	1/3	2/9	1/3	8.3±3.7	7.3±3.5
11	$Si_2B_3CN_3$	270	2.57	2/9	1/3	1/9	1/3	8.8±4.2	7.5±3.5
12	$Si_3B_2CN_2$	288	2.61	3/8	1/4	1/8	1/4	9.2±3.8	8.5±3.5
13	Si_3BC_2N	252	2.66	3/7	1/7	2/7	1/7	8.7±3.5	8.1±3.7

composition-dependent structural characteristics and bonding preferences, together with their correlation to thermodynamics and mechanical properties, are clarified. This work explores the complex relationships among compositions, the structural features, and the mechanical properties, being expected to inspire the innovation and advance in the study of SiBCN materials.

2 Methodology

2. 1 Calculation details

The structure and energy calculations are implemented using the Vienna *Ab-initio* Simulation Package (VASP) based on density functional theory (DFT) [25]. The projector-augmented wave (PAW) [26] and generalized-gradient approximation (GGA-PBEsol) functional [27] is employed as the exchange correlation functional. The cut-off energy for the plane-wave basis is set to 400 eV. The Brillouin zone of amorphous structures is sampled by a single *k*-point at gamma [28], and that of crystalline models is chosen with appropriate meshes of ~0.07 Å^{-1}. The convergence criterion for structure optimization is the force on each atom less than 1×10^{-2} eV/atom, and that for electronic minimization is 1×10^{-6} eV/atom. Throughout the creation and optimization of amorphous structures, the *ab-initio* molecular dynamics (AIMD) simulations under the canonical ensemble are employed. The time step is set to 2 fs for integrating the equations of motion and controlling temperature via rescaling the velocity every time step.

2. 2 Modeling of amorphous SiBCN structures

To balance the number of containing atoms and the computational costs, we generate three independent supercell sizes for the studied 13 compositions in accordance with their stoichiometric ratios. As listed in Table 1, there are 288 atoms contained in the supercells of compositions labeled 9 and 12, while there are 270 atoms for the compositions labeled 3, 4, 5, 10, and 11 and 252 atoms for the others. Their initial structures are generated by randomly distributing Si, B, C, and N atoms in the simulation boxes, in which the periodic boundary conditions are imposed on the systems. Meanwhile, their initial density is set to 2.52 g/cm³ referring to the experimental bulk SiBCN materials [29]. The amorphous structures of SiBCNs are created via the melt-quench algorithm, followed with the relaxation processes at a constant temperature. It is performed in three stages: (1) liquid mixing—The as-constructed simulation boxes are melted at 5000 K for 20 ps to break the initial configurations. The melt temperature of 5000 K ensures the formation of liquid phase for all compositions in the efficient manner [30]. (2) Quenching—The liquid structures are then cooled to 300 K in 20 ps. This quenching time is longer than the values in Refs. [11,31]. Reference [20] also shows that it is long enough since the energy change becomes ignorable with further increasing the quenching time.

(3) Atomic position and volume relaxation—The geometry optimization starts after the quenching procedure, and then runs for 6 ps. The final box volumes are obtained by fitting the calculated energies from 10 and/or more different volumes to the Birch–Murnaghan equation of state. The structures with final determined volumes are then optimized for another 6 ps at 300 K to fully relax the atoms. The validity of the algorithm settings and the reliability of the as-constructed amorphous structure have been discussed and established in Ref. [20]. For the energy and the atomic position analysis, the data are averaged over the final 500 snapshots taken from the dynamic simulations in corresponding sections.

2. 3 Mechanical property calculations

The second-order elastic constants together with the bulk (B), shear (G), and Young's moduli (E) are important parameters, revealing the structural response of a material to the external stress. For amorphous structures, there are only two independent elastic constants (c_{11} and c_{12}) as a result of their isotropic characteristics [32]. They can be calculated based on the stress–strain relationships through making a series of distorted structures with constrained geometry optimizations [33]. Here, three strain patterns and six deformation amplitudes up to 0.01 for each strain pattern are applied. For each studied composition, the determination of stress follows the approach by averaging the stresses of the 100 snapshots from the stimulation process. Then, c_{11} and c_{12} are calculated though averaging the three corresponding parameters along different orientations (c_{ij}), which aims to minimize the anisotropic influence originating from the adopted limited size supercell.

$$c_{11} = \frac{c_{11} + c_{22} + c_{33}}{3} \tag{1}$$

$$c_{12} = \frac{c_{12} + c_{23} + c_{13}}{3} \tag{2}$$

And c_{44} is evaluated by Eq. (3):

$$c_{44} = \frac{c_{11} - c_{12}}{2} \tag{3}$$

The bulk and shear moduli are estimated within the Voigt–Reuss–Hill approximation [34–36]. The Voigt and Reuss approximations define their upper and lower bounds. In the Voigt approximation, the bulk (B_V) and shear (G_V) moduli are

$$B_V = \frac{c_{11} + 2c_{12}}{3} \tag{4}$$

$$G_V = \frac{c_{11} - c_{12} + 3c_{44}}{5} \tag{5}$$

In the Reuss approximation, the bulk (B_R) and shear (G_R) moduli are

$$B_R = \frac{1}{3s_{11} + 6s_{12}} \tag{6}$$

$$G_R = \frac{5}{4(s_{11} - s_{12}) + 3s_{44}} \tag{7}$$

where s_{ij} is the compliance tensor and is calculated as the inverse of the stiffness matrix ($S = C^{-1}$). Hill [36] suggests the average of Voigt and Reuss values as a satisfactory approximation to the experimental moduli. Accordingly, the B, G, and E are obtained by Eqs. (8)–(10):

$$B = \frac{B_V + B_R}{2} \tag{8}$$

$$G = \frac{G_V + G_R}{2} \tag{9}$$

$$E = \frac{9BG}{3B + G} \tag{10}$$

It is reported that the elastic properties show a strong correlation with the composition of ceramics, but are relatively insensitive to their configurations [37]. Meanwhile, the influence of different initial atomic distributions on the bulk moduli has been tested by five samples of Si$_2$BC$_3$N. The deviation is small and does not influence the conclusions obtained in this work. To save the computational costs, one sample is finally adopted for the mechanical property calculations. The Vickers hardness (HV) of SiBCN materials is estimated using the empirical relation as [38]:

$$HV = 2(k^2 G)^{0.585} - 3 \tag{11}$$

where k is the Pugh's ratio defined as $k = G/B$.

3 Results and discussion

3. 1 Models of SiBCN ceramics

The studied 13 different compositions locate in the Si–BN–C quasi-ternary slice of the quaternary Si–B–C–N diagram, as illustrated in Fig. 1. The total atomic number (n) and the ratio of the four elements in these materials are provided in Table 1. The models of

four representative compositions are exhibited in Fig. 1. Schematic views for other compositions are available in Fig. S1 in the Electronic Supplementary Material (ESM). The density values after the volume optimization procedure are slightly higher than those after the initial set, ranging from 2.53 to 2.67 g/cm³. The randomization of the as-constructed 13 amorphous structures is supported by two facts. The one is the long atomic displacements during the melt-quench procedure. The average atomic displacements exceed 7.5 Å during the liquid mixing procedure and are over 6.9 Å during the quenching procedure, as summarized in Table 1. Namely, the structures have been rebuilt after the melt-quench procedure under the aforementioned calculation methodology. The other is the disorder atomic distribution, which is recognized from their radial distribution functions (RDFs), or $g(r)$. As shown in Fig. 2, the shapes of $g(r)$ showing the typical liquid-like features indicate the expected loss of long-range order, uncovering the amorphous feature of the as-constructed structures.

The RDF and partial distribution function (PDF) analyses are effective methods on presenting the characteristics of the modeled systems. The $g(r)$ is defined as

$$g(r) = \frac{n}{4\pi r^2 V} \times \frac{dn(r)}{dr} \qquad (12)$$

where V is the volume of the box, $dn(r)$ is the number of atoms at a distance between r and $r + dr$. The $g(r)$ gives the probability of finding an atom in a shell of thickness (dr) at a distance (r) from a reference point. As shown in Fig. 2, the RDFs of all the studied SiBCN ceramics have the first peak located between 1.5 and 2.23 Å. The first minimum of the RDF (FMRDF) is determined to be 2.23 Å. The first peak of some particular compositions consists of a relatively sharp main peak with a shoulder, such as SiB_2CN_2, $SiBC_4N$, and $Si_2B_3CN_3$. However, for the other compositions including $SiBC_2N$, Si_4BCN, Si_2BC_3N, Si_3BC_2N, and $Si_3B_2CN_2$, a splitting of the first peaks occurs. Such difference is attributed to the local unit variation, as discussed in Section 3.2.

The bonding analysis is based on the PDFs of atomic pairs (Fig. S2 in the ESM), together with considering the FMRDF and the bonds in typical crystal materials. The PDF of two chemical species ($g_{\alpha\beta}(r)$) is calculated by Eq. (13):
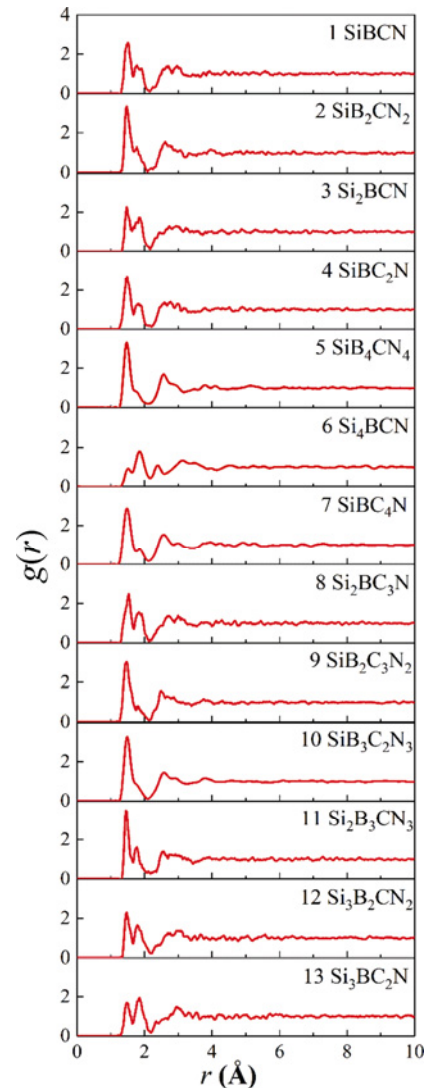

Fig. 2 Radial distribution functions of the studied amorphous SiBCN ceramics.

$$g_{\alpha\beta}(r) = \frac{nc_\alpha}{4\pi r^2 V} \times \frac{dn_{\alpha\beta}(r)}{dr} \qquad (13)$$

where c_α represents the concentration of α atomic species. The functions $g_{\alpha\beta}(r)$ refers to the probability of finding an atom of type β at a distance r from the reference α atom. The bond length cut-off (BLC) for each atomic pair is determined from the first minimum of corresponding PDFs. It should be noticed that the first peak may overlap with the second peak for several atom pairs (Si–Si, B–B, and Si–B), and thus their BLCs are determined only from the compositions without such overlapping. Seven types of chemical bonds can be identified since their BLCs (Table 2) are less than the FMRDF, including the Si–C bond, Si–N bond, B–C bond, B–N bond, C–C bond, C–N bond,

Table 2 Average bond lengths in amorphous SiBCN ceramics, cut off distances for each type of chemical bond, and the corresponding bond lengths in typical crystal materials (Unit: Å)

	Composition	Bond type								
		Si–Si	Si–B	Si–C	Si–N	B–C	B–N	C–C	C–N	B–B
1	SiBCN	2.39	2.10	1.90	1.79	1.59	1.49	1.48	1.44	1.69
2	SiB_2CN_2	2.41	2.08	1.90	1.77	1.59	1.48	1.50	1.46	1.69
3	Si_2BCN	2.38	2.11	1.91	1.79	1.58	1.47	1.53	1.45	1.76
4	$SiBC_2N$	2.36	2.05	1.91	1.79	1.61	1.48	1.47	1.41	1.79
5	SiB_4CN_4	—	2.12	1.91	1.79	1.61	1.49	1.54	1.42	1.89
6	Si_4BCN	2.39	2.05	1.90	1.79	1.59	1.48	1.51	—	1.72
7	$SiBC_4N$	2.33	2.08	1.92	1.77	1.60	1.50	1.48	1.43	—
8	Si_2BC_3N	2.34	2.04	1.91	1.79	1.59	1.51	1.47	1.44	—
9	$SiB_2C_3N_2$	2.38	2.08	1.92	1.78	1.62	1.48	1.47	1.40	1.78
10	$SiB_3C_2N_3$	2.29	2.10	1.89	1.78	1.61	1.49	1.46	1.45	1.75
11	$Si_2B_3CN_3$	2.43	2.10	1.90	1.78	1.60	1.49	1.52	1.46	1.74
12	$Si_3B_2CN_2$	2.39	2.06	1.91	1.80	1.59	1.47	1.52	—	1.82
13	Si_3BC_2N	2.40	2.10	1.91	1.80	1.60	1.47	1.47	1.36	1.79
	Cut-off distance	2.59	2.33	2.17	2.09	2.0	1.90	1.86	1.76	2.09
	Corresponding bond length in crystal	2.35[a]	2.06[b]	1.90[c]	1.73; 1.74[d]	1.66[e]	1.44[f]	1.55; 1.46[g]	1.33; 1.46[h]	1.67–1.80[i]

Note: [a] in Si crystal, Ref. [42]; [b] in SiB_6, Ref. [43]; [c] in β-SiC, Ref. [44]; [d] in β-Si_3N_4, Ref. [45]; [e] in B_4C, Ref. [46]; [f] in hexagonal-BN (h-BN), Ref. [47]; [g] 1.55 in diamond and 1.46 in graphite, Ref. [48]; [h] in C_3N_4, Ref. [49]; and [i] in B crystal, Ref. [50].

and B–B bond. For the Si–B pair, its BLCs are a little larger than the FMRDF, while its first peak mainly locates below the FMRDF. Only the atomic pairs with the *r* being less than FMRDF can form bonds. Meanwhile, the average bond lengths of the above eight bonds are similar to the corresponding bond lengths in crystal materials (Table 2). In the case of Si–Si pair, its BLC is 2.59 Å. Although this value is larger than the FMRDF (Table 2), it is comparable to the BLC (2.58 Å) of Si–Si bonds in amorphous Si [39]. Meanwhile, the calculated average Si–Si bond lengths based on this BLC are close to the Si–Si bond length in crystal Si (2.35 Å) and also close to that in amorphous Si (2.36 Å). Therefore, the Si–Si bond should form in the studied ceramics. However, the case of N–N pair is different. Its BLC (3.15 Å) is larger than both the FMRDF and the N–N bond (1.18 Å) in N_2 [40], indicating that the N–N bond does not form. Nine types of bonds are identified finally, which are also experimentally found at different stages of the structural evolution and/or in different preparation processes of SiBCN materials [3,4,7,41]. Six bonding types (Si–C, Si–N, Si–B, B–C, B–N, and C–C bonds) are shared in common for all compositions, while the C–N bond, Si–Si bond, and B–B bond are absent in several particular compositions, as listed in Table 2.

3. 2 Chemical bonds and local structures of SiBCN ceramics

It is of fundamental importance to illustrate the bonding changes that reflect the systematic evolution of structural characteristics and properties [32,51,52]. Figure 3 illustrates the bond statistics of the as-constructed amorphous structures, in which the percentage value beyond 3% are labeled. The identified nine types of chemical bonds form the SiBCN systems with different proportions, and the variation of bond percentage tends to be composition-dependent. Meanwhile, four bond types hold the large proportion for all compositions (B–C, Si–N, Si–C, and B–N bonds). For the compounds occupying the center area of the quasi-ternary diagram (including SiBCN, SiB_2CN_2, Si_2BCN, and $SiBC_2N$), the aforementioned four types of bonds are statistically in relative equilibrium. When the composition moves towards the outer area of the ternary diagram, the content fluctuation of the constituting elements leads to the growth of preferred chemical bond ratios. The SiB_4CN_4, Si_4BCN, and $SiBC_4N$ are representative compositions for the BN-rich portion, the Si-rich portion, and the C-rich portion within the Si–BN–C ternary diagram, respectively. For the BN-rich SiB_4CN_4, the proportion of B–N bond
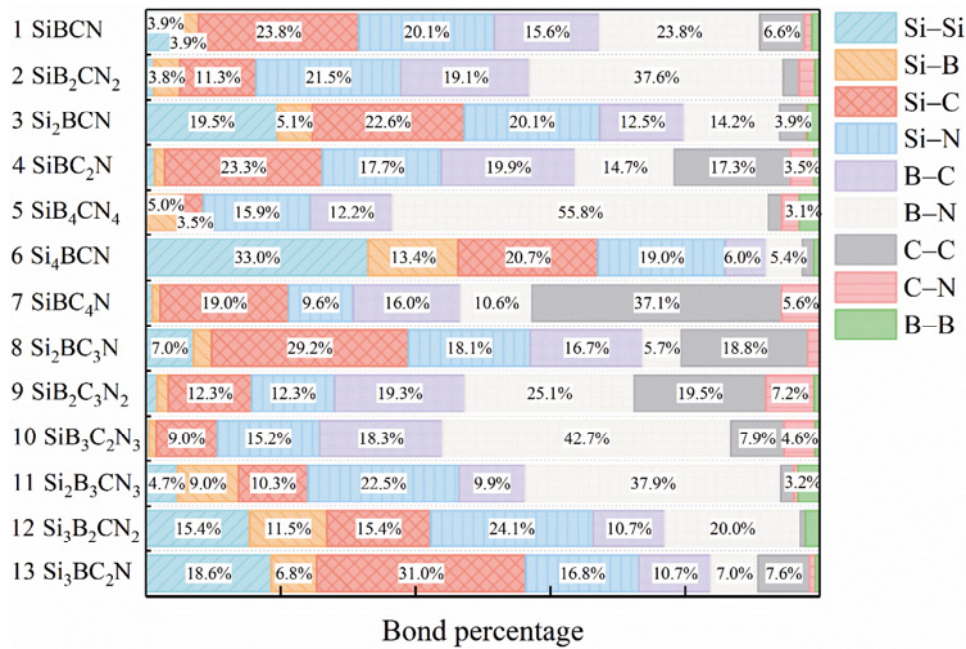
Fig. 3   Bond distribution statistics for SiBCN ceramics.

raises to 55.8%, which is 32.0% higher than that in SiBCN and 18.2% higher than that in SiB_2CN_2, manifesting that the boron and nitrogen atoms have the natural tendency to form the B–N bond. Similarly, the increased Si content brings the increment of Si-contained bonds from 51.7% in SiBCN to 67.3% in Si_2BCN and 86.1% in Si_4BCN, accompanying with the reduced tendency of the residual three elements forming bonds with each other. For the C-rich compound $SiBC_4N$, the C–C bond dominates with the highest bond proportion of 37.1%, while the Si–C bond and the B–C bond amount to 19.0% and 16.0%, respectively. If compared with that of SiBCN, the increased carbon content of $SiBC_4N$ results in the increment percentage of C–C bond from 6.6% to 37.1%, while it descends the proportion of Si–Si/B–B bond at the same time. It is reported that Si-contained bonds are weaker than those formed among B, C, and N, and thus the increment of its percentage may decrease the stiffness of SiBCN ceramics [20]. In the case of bonds among B, C, and N, although they are relatively strong, their contents are closely related to the percentage of easily distorted sp^2-like trigonal configurations. Therefore, the balance among the weak Si-contained bonds and soft sp^2-like trigonal configurations (i.e., bonds among B–C–N) through tailoring composition is expected an effective way of mechanical property optimization, as presented in Section 3.4.

The charge transfer of the constituent elements (*i*) in SiBCN ceramics is associated with the electronegativity and to some extent reflects the nature of the chemical bond. Bader charge analysis is an intuitive way to qualify the charge transitions and determine the efficient valence electrons by introducing the zero-flux surface, on which the charge density is identified as the minimum perpendicular to the surface [53]. The statistical analysis results of Bader charges are illustrated into ternary contour mappings, as shown in Fig. 4. For all studied SiBCN ceramics, the Si and B atoms tend to be positively charged, while the C and N atoms are negatively charged. The average charges for Si and B atoms distribute in the range of $+1.35e$–$+2.61e$ and $+0.30e$–$+1.96e$, respectively, whereas the distribution region is from $-2.29e$ to $-0.56e$ for C atoms and from $-2.20e$ to $-1.89e$ for N atoms. Namely, the Si atoms and B atoms tend to act as the electron donors, while the C atoms and N atoms prefer to be the electron receivers. The Bader charges for the concerned atoms are correlated with the type and concentration variation of chemical bonds in SiBCN systems, and thus display universal composition-dependent preferences in relatively wide ranges.

The structural stability and mechanical properties of materials are correlated with their local structural units. The combination of complex chemical bonds produces two types of polyhedral configurations in SiBCN ceramics, i.e., the sp^3-type tetrahedral configuration and the sp^2-like
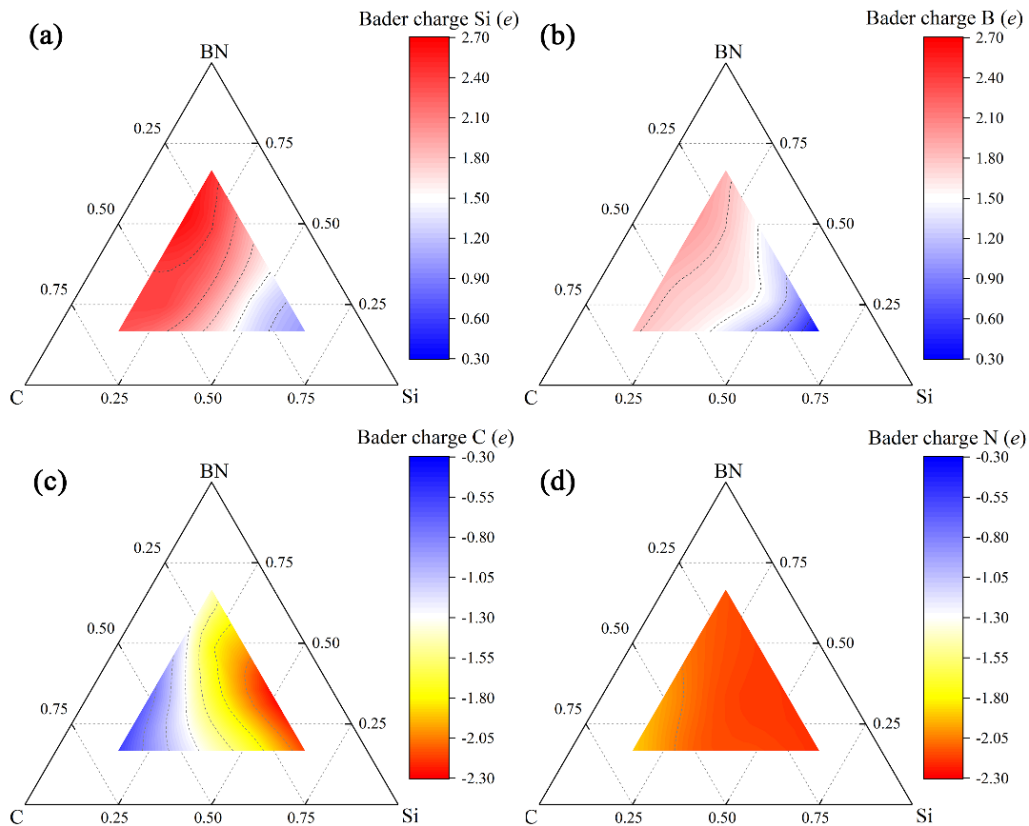
Fig. 4 Ternary contour mappings of Bader charge statistics for individual elements in amorphous SiBCN ceramics.

trigonal configuration [20]. The contribution of the componental element to the polyhedral configuration changes with the undulation of stoichiometry. In summary, the percentage of tetrahedral configuration in the amorphous structure decreases from the maximum value of 68.3% for Si$_4$BCN located at the Si-rich corner to around 40% at the Si-poor edge (SiB$_4$CN$_4$, SiBC$_4$N, SiB$_2$C$_3$N$_2$, and SiB$_3$C$_2$N$_3$). The sp^2-like trigonal configuration fluctuates in perfect opposition. In Fig. 5, the components of the above two polyhedron types are separately illustrated according to the central element. It is obvious that the silicon tends to form tetrahedral configuration in all compositions, and the ratio of Si-centered tetrahedra increases with the Si concentration. However, the boron and nitrogen scarcely form tetrahedra, and their proportions of the tetrahedral configuration vary within a small range regardless of the change of composition. A positive correlation is also observed between the B-/N-centered trigonal coordination polyhedra and BN content. The polyhedron formation preference shows flexibility in the case of carbon. The enhancement of carbon content induces the obvious increment of sp^2-like C-centered trigonal coordination polyhedra. Correspondingly, the

percentage of C-centered trigonal coordination polyhedra is higher than that of C-centered tetrahedra under C-rich conditions, while they are comparable in the residual composition area. Being differently, the formation of C-centered tetrahedra configuration competes with that of Si at the BN-rich corner, while the preferred C-centered trigonal configuration is negatively influenced by the B-/N-centered trigonal coordination polyhedra at the Si-rich corner. Such phenomenon is reasonable as these two units are the predominant structures in classical carbon phases of graphite and diamond.

The increment of the tetrahedral coordination proportion also leads to the evolution of the first peaks in RDFs, as revealed in Section 3.1. As the proportion of tetrahedral configuration in the amorphous structure rises from 35.2% in SiB$_3$C$_2$N$_3$ to 68.3% in Si$_4$BCN, the shoulder peak that represents the number of bonds in tetrahedral coordination grows up and finally becomes the sub-peak. Moreover, the wideness of second peaks is observed in all compositions, uncovering the large distortion of the polyhedron networks. This phenomenon originates from two facts. The first one is related to heterogeneous local units, i.e., the sp^2-like trigonal and
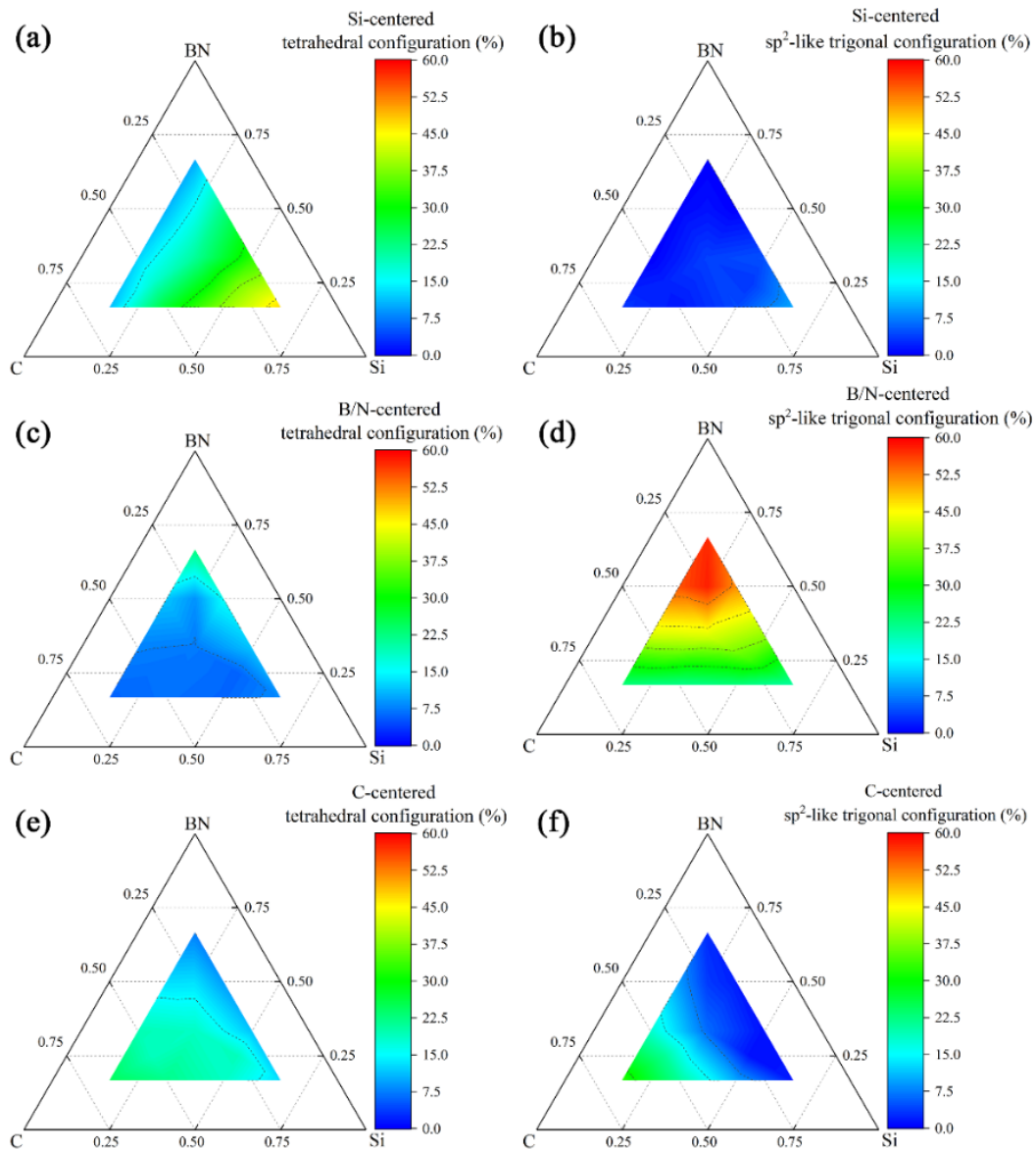
Fig. 5 Ternary contour mappings of composition-dependent (a, c, e) tetrahedral and (b, d, f) trigonal configuration statistics for individual elements in amorphous SiBCN ceramics.

the tetrahedral units as mentioned above. The second is the nesting of existing polyhedra in amorphous SiBCN ceramics [54]. These uncovered local units of all elements together with their concentration variation enrich the SiBCN ceramic family in a wide composition range. As the sp²-like trigonal configuration is associated with turbostratic carbon and BN stacks in SiBCN ceramics at high temperatures, these local structure results may shed light on understanding the high-temperature stability of SiBCN ceramics with different atomic ratios. Furthermore, it also partially contributes to the understanding of the mechanical properties, as discussed in Section 3.4.

3. 3 Thermodynamics of SiBCN ceramics

The cohesive energy (E_c) that expresses the potential wall of the chemical bonding is often adopted to predict the thermodynamic stability of materials. Here, it is calculated by Eq. (14) [55,56]:

$$E_c = E_t - n_{Si}\mu_{Si} - n_B\mu_B - n_C\mu_C - n_N\mu_N \qquad (14)$$

where E_t is the total energy of each SiBCN compound, μ_i is the atomic chemical potential of i, and n_i is the number of atom i in the compound. The μ_i is obtained by calculating the energy of one atom in the center of box with the size of 10 Å × 10 Å × 10 Å. The negative calculated cohesive energy values, as summarized in

Table 3, reveal that the formation of chemical bonds in the related amorphous SiBCN ceramics is thermodynamically driven. Meanwhile, their absolute values are associated with the global bond strengths of these compounds, and will also play an important role on their mechanical properties.

The formation energy is a reference to identify whether a reaction occurs easily or with difficulty. Based on the elemental molar ratios of the considered SiBCN compositions, the formation energy is evaluated along two different reaction pathways. In the first path, Si, graphite, and BN are considered to provide silicon, carbon, and B/N elements, respectively. Meanwhile, SiC and BN, as commercially available binary ceramics, are adopted in the second route, together with Si (for Si_2BCN, Si_4BCN, $Si_2B_3CN_3$, Si_3BC_2N, and $Si_3B_2CN_2$) or graphite (for $SiBC_2N$, $SiBC_4N$, Si_2BC_3N, $SiB_2C_3N_2$, and $Si_3B_2CN_2$) in certain compounds for satisfying their elemental molar ratios. For SiC, Si, BN, and graphite, the atomic position and volume are optimized using the same procedure, as described in the third stage of the amorphous structure construction procedure by the AIMD simulations. Then, the ΔH_f is calculated by Eq. (15):

$$\Delta H_f = E_t - \sum_{i=1} m_i E_i \qquad (15)$$

where E_i and m_i are the energy and fraction of the reactants, respectively. The calculated formation energies,

together with the adopted reactants and compositions, are collected and compared in Table 3. The highest formation energy appears for $SiBC_4N$ (at the C-rich corner in the ternary diagram), while the lowest value occurs for Si_4BCN (at the Si-rich corner in the ternary diagram). Moreover, it is revealed that the incorporation of SiC would significantly increase the formation enthalpies of SiBCN ceramics. In other words, the formation energies on taking Si, graphite, and BN as the source of constituents are the proper choice from the energetic point of view, which is validated by the fact that these three compounds are commonly used for the fabrication of SiBCN amorphous ceramics based on mechanical alloying processing routes [57,58].

3. 4　Mechanical properties of SiBCN ceramics

The second-order elastic constants, together with the bulk, shear, and Young's moduli, are determined by the bonding strength near the equilibrium volume, representing the response of chemical bonds to the externally applied load within the elastic deformation limit. Table 4 summarizes the calculated second-order elastic constants for all focused amorphous SiBCN ceramics. It is seen that they tend to possess large tensile deformation-related c_{11} but the small shear distortion-related c_{12} and c_{44}. The value of the former (c_{11}) is in the range from 174 to 277 GPa, while those for the latter two parameters (c_{12} and c_{44}) are in the range of 60–103 and 56–89 GPa, respectively.

Table 3　Calculated cohesive energy and reaction path that dependent formation energies (ΔH_f). The reactants include Si, SiC, graphite (C), and BN

	Composition	E_c (eV/ atom)	Reaction path			
			Reactant	ΔH_f (eV/ atom)	Reactant	ΔH_f (eV/ atom)
1	SiBCN	−7.69	Si+C+BN	0.49	SiC+BN	0.59
2	SiB_2CN_2	−7.80	Si+C+2BN	0.51	SiC+2BN	0.58
3	Si_2BCN	−7.09	2Si+C+BN	0.47	SiC+BN+Si	0.55
4	$SiBC_2N$	−7.77	Si+2C+BN	0.59	SiC+BN+C	0.67
5	SiB_4CN_4	−7.77	Si+C+4BN	0.54	SiC+4BN	0.59
6	Si_4BCN	−6.38	4Si+C+BN	0.41	SiC+BN+3Si	0.47
7	$SiBC_4N$	−7.82	Si+4C+BN	0.66	SiC+BN+3C	0.72
8	Si_2BC_3N	−7.38	2Si+3C+BN	0.54	2SiC+BN+C	0.66
9	$SiB_2C_3N_2$	−7.78	Si+3C+2BN	0.63	SiC+2BN+2C	0.68
10	$SiB_3C_2N_3$	−7.81	Si+2C+3BN	0.55	SiC+3BN+C	0.60
11	$Si_2B_3CN_3$	−7.41	2Si+C+3BN	0.51	SiC+3BN+Si	0.56
12	$Si_3B_2CN_2$	−6.94	3Si+C+2BN	0.49	SiC+2BN+2Si	0.54
13	Si_3BC_2N	−6.85	3Si+2C+BN	0.51	2SiC+BN+Si	0.63

Table 4　Summary for the calculated second-order elastic constants 　　　　　　　　(Unit: GPa)

	Composition	c_{11}	c_{12}	c_{44}
1	SiBCN	245	98	74
2	SiB_2CN_2	230	73	78
3	Si_2BCN	180	68	56
4	$SiBC_2N$	222	60	81
5	SiB_4CN_4	221	65	78
6	Si_4BCN	181	68	56
7	$SiBC_4N$	238	86	76
8	Si_2BC_3N [20]	245	88	78
9	$SiB_2C_3N_2$	277	99	89
10	$SiB_3C_2N_3$	260	103	78
11	$Si_2B_3CN_3$	217	79	69
12	$Si_3B_2CN_2$	174	63	56
13	Si_3BC_2N	198	64	67

The predicted mechanical properties of different SiBCN ceramics including the bulk, shear, Young's moduli, and *HV* are summarized in Table 5. It is obvious that the mechanical properties strongly correlate with the composition. The bulk moduli are in the range between 100 and 158 GPa, the shear moduli between 56 and 89 GPa, and the Young's moduli between 141 and 225 GPa. Experimentally, the reported mechanical properties of SiBCN materials distribute in a wide range for two reasons [57–59]. Firstly, no matter the SiBCN ceramics are fabricated by the polymer precursor-derived ceramic processing and/or the mechanical alloying inorganic processing routes, the precise stoichiometric ratio of SiBCN samples is very difficult to be precisely measured. Secondly, fully dense single-phase SiBCN samples are hardly to be obtained by conventional sintering routes as a result of the strong covalent bonds with low diffusion coefficients of the constituting elements even at high temperatures. Therefore, the range of mechanical properties is adopted for comparison here. The experimental Young's moduli of SiBCN materials range between 91 and 291 GPa [57–59], which are consistent with our calculated ones ranging from 141 to 225 GPa. Similar situation emerges when it turns to the calculated *HV*, ranging from 7 to 14 GPa, being comparable to the experimental values varying from 1.6 to 15.0 GPa [23,60]. Accordingly, our computed results and the experimental reference data from recent literatures are in good agreement.

Table 5 **Summary for the calculated mechanical properties, including bulk modulus (*B*), shear modulus (*G*), Young's modulus (*E*), Pugh's ratio (*k*), and Vickers Hardness (*HV*)**

	Composition	*B* (GPa)	*G* (GPa)	*E* (GPa)	*k*	*HV* (GPa)
1	SiBCN	147	74	190	0.50	8
2	SiB$_2$CN$_2$	125	78	195	0.63	12
3	Si$_2$BCN	105	56	143	0.54	7
4	SiBC$_2$N	114	81	196	0.71	14
5	SiB$_4$CN$_4$	117	78	191	0.67	13
6	Si$_4$BCN	106	56	144	0.53	7
7	SiBC$_4$N	137	76	192	0.55	10
8	Si$_2$BC$_3$N [20]	140	78	197	0.56	10
9	SiB$_2$C$_3$N$_2$	158	89	225	0.56	11
10	SiB$_3$C$_2$N$_3$	155	78	201	0.50	9
11	Si$_2$B$_3$CN$_3$	125	69	175	0.55	9
12	Si$_3$B$_2$CN$_2$	100	56	141	0.56	8
13	Si$_3$BC$_2$N	109	67	167	0.62	10

As shown in Fig. 6, the mechanical properties of SiBCN ceramics possess a general compositional correlation. The high moduli within the studied compositions locate in the region with low Si contents together with fairly moderate C and/or BN contents (like SiB$_2$C$_3$N$_2$ and SiB$_3$C$_2$N$_3$ at the center of the C–BN edge). Meanwhile, the moduli decrease with the increasing Si, C, and BN contents. Si-rich compositions (like Si$_4$BCN and Si$_3$B$_2$CN$_2$) have low moduli within the studied series of compositions, while the C-rich (like SiBC$_4$N) and BN-rich (like SiB$_4$CN$_4$) compositions tend to have moderate values. Such variations of mechanical properties should originate not only from the composition-dependent type of
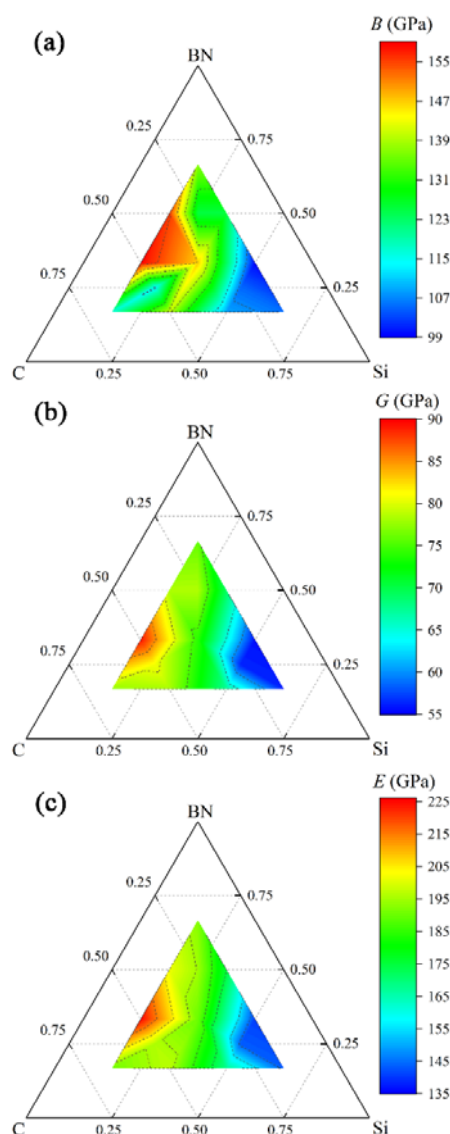

Fig. 6 Ternary contour mappings for calculated (a) bulk moduli, (b) shear moduli, and (c) Young's moduli of as-constructed amorphous structures.

chemical bonds, but also from the evolution of local polyhedral units [61–63]. An increasing amount of Si will result in the increment of Si-contained chemical bonds, which are longer than the chemical bonds formed among B, C, and N. The well participation of Si-contained bonds elongates the average bond length and reduces the bond strength of SiBCN ceramics, which contributes to the decrement of the mechanical properties. Moreover, such composition change will also increase the percentage of Si-centered tetrahedra as well as the proposition of the total tetrahedral configuration. Since Si-contained bond lengths are obviously different from those among B, C, and N, the increment of Si-contained bonds would increase the bond length deviations in tetrahedral configurations [20]. These tetrahedra with high Si-contained bond percentages have high deformation freedom, leading to their relatively weak effect on mechanical properties. These two combined phenomena account for the minimum moduli observed at Si-rich area. In the cases of high C- and/or BN-rich compositions, the effect of C-centered and B-/N-centered sp^2-like trigonal configuration becomes important, while the chemical bond strength may change less as a result of the similar bond lengths among B, C, and N. So, the decrement of moduli along C and/or BN content increasing directions is moderate.

The stress–strain relation reflects the universal feature of the mechanical properties of amorphous solids [64]. Since the strength isotropy of the amorphous SiBCN material has been clarified in Ref. [20], tensile/shear strengths along three equivalent directions are averaged for all of the studied compounds in this work. For both tensile/shear strength curves (Fig. S3 in the ESM), in the low strain region, the stress increases with the increment of strain and reaches the first peak when plastic deformation emerges. Then, the tensile strength curves decrease after the peak value, indicating elastic instability. In the case of the shear strength curves, the stresses fluctuate around the average value, in which the ongoing failure and re-formation of the chemical bonds occur [65]. Such plateau characteristic is ubiquitous for various amorphous solids, which are attributed to the variability of configurations [66,67]. In this region, the load bearing on the atomic scale occurs, and the response of weak bonds dominates the deformation [68].

The tensile/shear strengths of the studied compositions

are taken as the first peak in the stress–strain curves, and the corresponding average strength values of three directions are collected in Table 6. The tensile strength of the studied materials varies from 13.1±0.5 GPa (Si_4BCN) to 23.1±0.5 GPa ($SiB_2C_3N_2$), and the shear strength varies from 3.8±0.2 GPa (Si_4BCN) to 8.1±0.2 GPa ($SiB_2C_3N_2$). It is noticed that the increase of the Si content leads to a decrease in both tensile and shear strengths, which is in good agreement with the tendency of the composition-dependent moduli. The high percentage of Si, resulting in the formation of weak Si–Si bond and high contents of Si-centered tetrahedra, which obstructs the configuration evolution throughout the strain application, leads to low fracture resistance. The increased contents of C and BN enrich the configuration variety by introducing sp^2-like trigonal bonded C, N, and B and increase the percentage of strong bonds. The low tensile and shear strength values of SiBCN materials comparing to those of the corresponding binary covalent crystals (like SiC (101 GPa [69] or 88.17 GPa [70]) and Si_3N_4 (57 GPa along the [100] direction and 55 GPa for the [001] direction [71])) arise from their high flaw sensitivity to strain loading. Their low shear resistance supports the application of SiBCN materials as the thermal shock resistant ceramic matrix, e.g., for fiber-reinforced composite materials. Moreover, the plateau, in which the sustainability of this steady state region is composition-dependent, may be desirable for micro-structural devices under large strain loadings. The discovered mechanical characteristics of amorphous SiBCN materials are expected to inspire their further

Table 6   Tensile/shear strengths of SiBCN materials

	Composition	Tensile <100> (GPa)	Shear {(010) [100]} (GPa)
1	SiBCN	21.2 ± 2.7	6.1±0.3
2	SiB_2CN_2	20.6±1.9	6.3±0.5
3	Si_2BCN	16.8±3.1	4.4±0.6
4	$SiBC_2N$	21.9±2.2	7.0±0.2
5	SiB_4CN_4	20.7±2.5	6.7±0.8
6	Si_4BCN	13.1±0.5	3.8±0.2
7	$SiBC_4N$	22.4±1.8	7.3±0.6
8	Si_2BC_3N [20]	20.5±0.2	6.6±0.2
9	$SiB_2C_3N_2$	23.1±0.5	8.1±0.2
10	$SiB_3C_2N_3$	22.9±1.0	6.8±0.8
11	$Si_2B_3CN_3$	19.6±0.2	5.8±0.3
12	$Si_3B_2CN_2$	14.7±0.9	4.9±0.3
13	Si_3BC_2N	14.0±0.5	4.1±0.3

development for various structural and functional applications.

Both the calculated and experimental results suggest that SiBCN materials are suitable as the ceramic matrix for composites [72,73]. In ceramic-matrix composites, crack arrest or deflection at interfaces is beneficial to their damage tolerance, which requires interfaces that can be debonded. The interface region is a crucial part for the crack arrest and damage tolerance. The Cook and Gordon mechanism [74] has been widely accepted to evaluate the crack deflection, in which a semi-elliptical crack is placed in a material subjected to uniaxial tension. The stress state at the crack tip is revealed to be multiaxial, including the stress component (σ_{rr}) that is parallel to the crack plane (*r*-axis) and the stress component (σ_{zz}) that is perpendicular to the crack plane. Zhang *et al*. [19] and Pompidou and Lamon [75] developed the criteria for crack deflection at interfaces based on the Cook and Gordon mechanism. A crack initiating in Material 1 (matrix, Young's modulus E_1) propagates towards the uncracked Material 2 (E_2, strength σ_2^c). The distance from the crack tip to which is denoted l (ligament) when debonding occurs. The failure of interface occurs when two conditions are satisfied: (1) The stress at distance l ahead of crack tip exceeds the interface strength (σ_i^c), and (2) the stress is smaller than the strength of Material 2 at distance $> l$ so that the failure of Material 2 does not occur. Based on these conditions, the debonding criterion can be described as

$$\frac{\sigma_i^c}{\sigma_2^c} \leqslant \frac{\sigma_{rr}^{\max}}{\sigma_{zz}^{\max}(r > l)} \tag{16}$$

where $\sigma_{rr}^{\max}$ and $\sigma_{zz}^{\max}$ are the maximum of stress components σ_{rr} and σ_{zz}, respectively. The master

curve ($\frac{\sigma_{rr}^{\max}}{\sigma_{zz}^{\max}} = f\left(\frac{E_2}{E_1}\right)$) is derived from the relationships between the deflection criterion and Young's moduli, as presented in Fig. 7. Debonding occurs for the appropriate values of constituent properties (E_2/E_1 and σ_i^c / σ_2^c) lying in the domain under the master curve. σ_i^c / σ_2^c appraises the debonding potential of the interface, which can be predicted with a certain E_2/E_1 ratio. Moreover, once E_1, E_2, and σ_2^c are available, σ_i^c can be estimated. The upper limit of σ_i^c for debonding is defined as the interface debonding strength (σ_i^{c+}). The higher the σ_i^{c+}, the higher interface debonding capability.

In this work, the debonding potential of C_f/SiBCN and SiC_f/SiBCN (the subscript f means fiber) interfaces are predicted [76,77]. The Young's moduli of C_f and SiC_f refer to 349 and 280 GPa, respectively [75], while their σ_i^c are 2845 and 1500 MPa, respectively [78]. When a particular fiber constituent is set, the E_2/E_1 ratios of SiBCNs distribute within the region, which are determined by the corresponding values of $SiB_2C_3N_2$ (bottom limit) and $Si_3B_2CN_2$ (upper limit), as shown in Fig. 7. It can be predicted that cracks in the SiBCN matrix are more likely to deflect at the interface for both C_f/SiBCN and SiC_f/SiBCN composites, which are consistent with the observed non-brittle fracture reported in Ref. [79]. The σ_i^{c+} of C_f/SiBCNs interface (e.g., 2048 MPa for the C_f/SiB$_2$C$_3$N$_2$ interface) is larger than that of SiC_f/SiBCNs interface (e.g., 885 MPa for the SiC_f/SiB$_2$C$_3$N$_2$ interface), as listed in Table S1 in the ESM, indicating that the debonding is highly probable at the C_f/SiBCN interface. Introduction of a compliant interphase (like pyrolytic carbon (PyC)) is one of the popular fiber surface treatments, which changes the
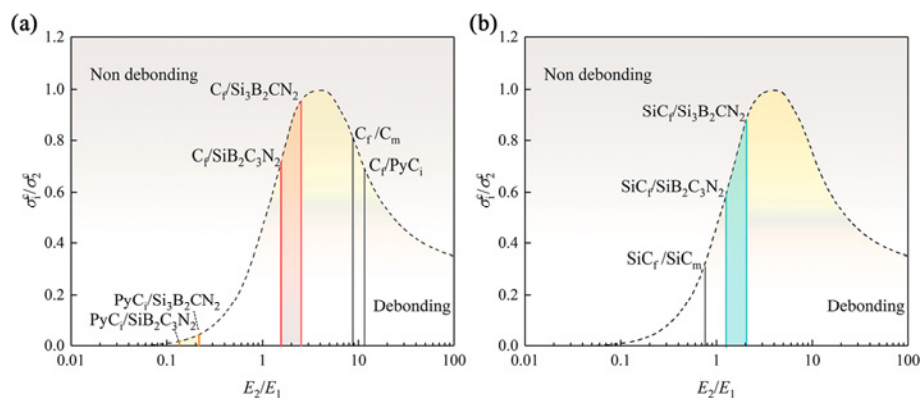

Fig. 7 Prediction of the possibility for crack deflection in Cf/SiBCNs and SiCf/SiBCNs composites based on Cook and Gordon model [75]. f, i, and m refer to fiber, interphase, and matrix, respectively.

crack propagation in the composite at the same time. Considering the case of $C_f/PyC_i/SiBCN$ (the subscript i means interphase), the debonding potential at the C_f/PyC_i interface is higher than that at the $PyC_i/SiBCN$ interface, indicating that the former is the favorable location for debonding (the Young's moduli and strength of PyC interface refer to 30 GPa and 151 MPa, respectively [75]). For the studied SiBCN materials, the rise of the Si content would decrease the Young's modulus, and therefore improve the debonding capability of the $C_f/SiBCN$ (or $SiC_f/SiBCN$) interface. Moreover, the crack deflection is also related to the thermal shock resistance of materials [80,81]. During thermal cycling, the capability to resist crack propagation caused by thermal shock is proportional to the Young's modulus. Therefore, the SiBCN compositions in the region with low Si contents and fairly moderate C and/or BN contents (like $SiB_2C_3N_2$ and $SiB_3C_2N_3$) have relatively high mechanical properties (including elastic moduli and debonding potential), indicating an improvement in thermal shock resistance, which should be suitable for the applications requiring high stiffness.

4 Conclusions

In this work, amorphous silicoboron carbonitride ceramics with 13 different compositions are modelled, and their thermodynamic stability, local structural variations, bonding characteristics, and mechanical properties are studied. All these ceramics have negative cohesive energies but positive formation energies, revealing that amorphous SiBCN ceramics can form and are energetically metastable. Meanwhile, Si, graphite, and h-BN are found to be the proper reactants as a result of the relatively low formation energies, being consistent with the mechanical alloying synthesis of SiBCN compositions.

The Si and B atoms tend to show positively charged in the studied materials, while both the C and N atoms are negatively charged. Nine types of chemical bonds are identified, and their content varies with the composition of the constituting elements. Among them, B–C, Si–N, Si–C, and B–N bonds hold the large proportion for all compositions. The silicon tends to form tetrahedral coordination, while the boron and nitrogen prefer the sp^2-like trigonal configuration. The positive correlation is observed in the above

elemental-configuration relationships for all compositions. However, carbon shows the flexible polyhedron formation preference. The C-centered trigonal coordination polyhedra are predominant under C-rich conditions, while trigonal and tetrahedral configurations are comparable for others. The composition dependence of bond distribution could be summed in two aspects. One is the increasing percentage of Si-contained bonds accompanied with the increment of Si content. It results in the raising bond length deviations and the enhancement of distortion of the polyhedral units. The other is the increasing amount of sp^2-like trigonal bonded C, N, and B introduced by the increase of C and/or B/N contents. Such local units of each element together with their concentration variation enrich the Si–B–C–N ceramic family in a wide composition range.

Composition-dependent mechanical properties are predicted. All the parameters, including the elastic constants, bulk, shear, and Young's moduli, together with tensile/shear strengths, are influenced by composition-dependent chemical bonds and the evolution of local polyhedral units. Mechanical properties are relatively high in general for compositions located in the region with low Si contents together with fairly moderate C and/or BN contents, and decrease along with the increasing amounts of Si, C, and BN contents. The decreasing trend can be attributed to the following two reasons: (1) Increasing the Si content results in the increment of Si-contained chemical bonds, which results in the bond length elongation and the bond strength reduction, and (2) the effect of C-centered and B-/N-centered trigonal coordination polyhedra become important in high C- and/or BN-rich compositions. Moreover, amorphous SiBCN materials show high flaw sensitivity to strain loading, which results in lower tensile and shear strength values than those of the corresponding covalent crystalline counterparts. The debonding potential prediction suggests that the fiber/SiBCN interfaces in composites are prone to crack deflection. These results support the application of amorphous SiBCN ceramics as the thermal shock resistant ceramic matrix suitable for the fabrication of advanced composite materials. This work provides a comprehensive analysis among the composition dependence of the structural features and the mechanical properties. The obtained results will allow to guide the further advancement of SiBCN-based ceramics and composites for structural and functional

applications in harsh environments in particular in the fields of energy and transportation materials.

Acknowledgements

Electronic Supplementary Material

Supplementary material is available in the online version of this article at https://doi.org/10.26599/JAC.2023.9220733.

References

[1] Fahrenholtz WG. A historical perspective on research related to ultra-high temperature ceramics. In: *Ultra-High Temperature Ceramics: Materials for Extreme Environment Applications*. Fahrenholtz WG, Wuchina EJ, Lee WE, Eds. Hoboken, USA: John Wiley & Sons, Ltd., 2014: 6–32.

[2] Guo CY, Wang EH, Fang Z, *et al*. New design concept for stable α-silicon nitride based on the initial oxidation evolution at the atomic and molecular levels. *J Mater Sci Technol* 2022, **122**: 156–164.

[3] Riedel R, Kienzle A, Dressler W, *et al*. A silicoboron carbonitride ceramic stable to 2,000 ℃. *Nature* 1996, **382**: 796–798.

[4] Jia DC, Liang B, Yang ZH, *et al*. Metastable Si–B–C–N ceramics and their matrix composites developed by inorganic route based on mechanical alloying: Fabrication, microstructures, properties and their relevant basic scientific issues. *Prog Mater Sci* 2018, **98**: 1–67.

[5] Viard A, Fonblanc D, Lopez-Ferber D, *et al*. Polymer derived Si–B–C–N ceramics: 30 years of research. *Adv Eng Mater* 2018, **20**: 1800360.

[6] Paul A, Binner J, Vaidhyanathan B. UHTC composites for hypersonic applications. In: *Ultra-High Temperature Ceramics: Materials for Extreme Environment Applications*. Fahrenholtz WG, Wuchina EJ, Lee WE, Eds. Hoboken, USA: John Wiley & Sons, Ltd., 2014: 144–166.

[7] Wang BZ, Li DX, Yang ZH, *et al*. Microstructural evolution and mechanical properties of *in situ* nano Ta$_4$HfC$_5$ reinforced SiBCN composite ceramics. *J Adv Ceram* 2020, **9**: 739–748.

[8] Guan JY, Li DX, Yang ZH, *et al*. Ta(B,C,N) and (Ta,Mi)(B,C,N) (Mi = Nb, W) ceramics by high-energy ball milling: Processing and solution mechanisms. *J Am Ceram Soc* 2023, **106**: 699–708.

[9] Petrman V, Houska J, Kos S, *et al*. Effect of nitrogen content on electronic structure and properties of SiBCN materials. *Acta Mater* 2011, **59**: 2341–2349.

[10] Chen PG, Li W, Li XC, *et al*. Effect of boron content on the microstructure and electromagnetic properties of SiBCN ceramics. *Ceram Int* 2022, **48**: 3037–3050.

[11] Matas M, Prochazka M, Vlcek J, *et al*. Dependence of characteristics of Hf(M)SiBCN (M = Y, Ho, Ta, Mo) thin films on the M choice: *Ab-initio* and experimental study. *Acta Mater* 2021, **206**: 116628.

[12] Ren ZK, Mujib SB, Singh G. High-temperature properties and applications of Si-based polymer-derived ceramics: A review. *Materials* 2021, **14**: 614.

[13] Li DX, Yang ZH, Jia DC, *et al*. High-temperature oxidation resistance of dense amorphous boron-rich SiBCN monoliths. *Corros Sci* 2019, **157**: 312–323.

[14] Song CK, Ye F, Liu YS, *et al*. Microstructure and dielectric property evolution of self-healing PDC–SiBCN in static air. *J Alloys Compd* 2019, **811**: 151584.

[15] Rao LX, Liu H, Hu TS, *et al*. Relationship between bonding characteristic and thermal property of amorphous carbon structure: *Ab initio* molecular dynamics study. *Diam Relat Mater* 2021, **111**: 108211.

[16] Deringer VL, Bernstein N, Bartók AP, *et al*. Realistic atomistic structure of amorphous silicon from machine-learning-driven molecular dynamics. *J Phys Chem Lett* 2018, **9**: 2879–2885.

[17] Lobzenko I, Shiihara Y, Iwashita T, *et al*. Shear softening in a metallic glass: First-principles local-stress analysis. *Phys Rev Lett* 2020, **124**: 085503.

[18] Cui L, Wang QQ, Xu B, *et al*. Prediction of novel SiCN compounds: First-principles calculations. *J Phys Chem C* 2013, **117**: 21943–21948.

[19] Zhang SY, Liu M, Luo YX, *et al*. Theoretical prediction on structure evolution and optimal properties of silicon modified hexagonal boron nitride as interphase in SiC$_f$/SiC composite. *J Eur Ceram Soc* 2022, **42**: 5323–5333.

[20] Liu YC, Zhou Y, Jia DC, *et al*. Unveiling structural features and mechanical properties of amorphous Si$_2$BC$_3$N by density functional theory. *J Mater Sci Technol* 2023, **139**: 103–112.

[21] Tavakoli AH, Golczewski JA, Bill J, *et al*. Effect of boron on the thermodynamic stability of amorphous polymer-derived Si–(B–)C–N ceramics. *Acta Mater* 2012, **60**: 4514–4522.

[22] Liao NB, Xue W, Zhou HM, *et al*. Numerical investigation into the nanostructure and mechanical properties of amorphous SiBCN ceramics. *RSC Adv* 2013, **3**: 14458–14465.

[23] Yang ZH, Jia DC, Duan XM, *et al*. Effect of Si/C ratio and their content on the microstructure and properties of

Si–B–C–N Ceramics prepared by spark plasma sintering techniques. *Mater Sci Eng A* 2011, **528**: 1944–1948.

[24] Li DX, Yang ZH, Jia DC, *et al*. Role of boron addition on phase composition, microstructural evolution and mechanical properties of nanocrystalline SiBCN monoliths. *J Eur Ceram Soc* 2018, **38**: 1179–1189.

[25] Kresse G, Furthmüller J. Efficient iterative schemes for *ab initio* total-energy calculations using a plane-wave basis set. *Phys Rev B* 1996, **54**: 11169–11186.

[26] Kresse G, Joubert D. From ultrasoft pseudopotentials to the projector augmented-wave method. *Phys Rev B* 1999, **59**: 1758–1775.

[27] Perdew JP, Ruzsinszky A, Csonka GI, *et al*. Restoring the density-gradient expansion for exchange in solids and surfaces. *Phys Rev Lett* 2008, **100**: 136406.

[28] Monkhorst HJ, Pack JD. Special points for Brillouin-zone integrations. *Phys Rev B* 1976, **13**: 5188–5192.

[29] Zhang PF, Jia DC, Yang ZH, *et al*. Microstructural features and properties of the nano-crystalline SiC/BN(C) composite ceramic prepared from the mechanically alloyed SiBCN powder. *J Alloys Compd* 2012, **537**: 346–356.

[30] Marks NA. Evidence for subpicosecond thermal spikes in the formation of tetrahedral amorphous carbon. *Phys Rev B* 1997, **56**: 2441–2446.

[31] Houska J, Kos S. *Ab initio* modeling of complex amorphous transition-metal-based ceramics. *J Phys Condens Matter* 2011, **23**: 025502.

[32] Green DJ. *An Introduction to the Mechanical Properties of Ceramics*. Cambridge, UK: Cambridge University Press, 1998.

[33] Liu B, Liu YC, Zhu CH, *et al*. Advances on strategies for searching for next generation thermal barrier coating materials. *J Mater Sci Technol* 2019, **35**: 833–851.

[34] Voigt W. *Lehrbuch der Kristallphysik*. Leipzig, Germany: Teubner, 1928. (in German)

[35] Reuss A. Berechnung der fließgrenze von mischkristallen auf grund der plastizitätsbedingung für einkristalle. *J Appl Math Mech* 1929, **9**: 49–58. (in German)

[36] Hill R. The elastic behaviour of a crystalline aggregate. *Proc Phys Soc A* 1952, **65**: 349–354.

[37] Zhang YH, Liu B, Wang JM, *et al*. Theoretical investigations of the effects of ordered carbon vacancies in ZrC_{1-x} on phase stability and thermo-mechanical properties. *Acta Mater* 2016, **111**: 232–241.

[38] Chen XQ, Niu HY, Li DZ, *et al*. Modeling hardness of polycrystalline materials and bulk metallic glasses. *Intermetallics* 2011, **19**: 1275–1281.

[39] Meidanshahi RV, Bowden S, Goodnick SM. Electronic structure and localized states in amorphous Si and hydrogenated amorphous Si. *Phys Chem Chem Phys* 2019, **21**: 13248–13257.

[40] Pollock CJ, Grubel K, Holland PL, *et al*. Experimentally quantifying small-molecule bond activation using valence-to-core X-ray emission spectroscopy. *J Am Chem Soc* 2013, **135**: 11803–11808.

[41] Houška J, Čapek J, Vlček J, *et al*. Bonding statistics and electronic structure of novel Si–B–C–N materials: *Ab initio* calculations and experimental verification. *J Vac Sci Technol A* 2007, **25**: 1411–1416.

[42] Többens DM, Stüßer N, Knorr K, *et al*. E9: The new high-resolution neutron powder diffractometer at the Berlin neutron scattering center. *Mater Sci Forum* 2001, **378–381**: 288–293.

[43] Durandurdu M. Amorphous silicon hexaboride at high pressure. *Philos Mag* 2020, **100**: 1818–1833.

[44] Su W, Li YY, Nie C, *et al*. First principles study of the C/Si ratio effect on the ideal shear strength of β-SiC. *Mater Res Express* 2016, **3**: 075503.

[45] Boulay DD, Ishizawa N, Atake T, *et al*. Synchrotron X-ray and *ab initio* studies of beta-Si_3N_4. *Acta Crystallogr B* 2004, **60**: 388–405.

[46] Data retrieved from the Materials Project for B4C (mp-696746) from database version v2022.10.28. Available at https://doi.org/10.17188/1285041.

[47] Xu YN, Ching WY. Electronic, optical, and structural properties of some wurtzite crystals. *Phys Rev B* 1993, **48**: 4335–4351.

[48] Fayos J. Possible 3D carbon structures as progressive intermediates in graphite to diamond phase transition. *J Solid State Chem* 1999, **148**: 278–285.

[49] Data retrieved from the Materials Project for C3N4 (mp-570572) from database version v2022.10.28. Available at https://doi.org/10.17188/1275794.

[50] Data retrieved from the Materials Project for B (mp-160) from database version v2022.10.28. Available at https://doi.org/10.17188/1191505.

[51] Bai YL, Qi XX, Duff A, *et al*. Density functional theory insights into ternary layered boride MoAlB. *Acta Mater* 2017, **132**: 69–81.

[52] Duan XJ, Fang Z, Yang T, *et al*. Maximizing the mechanical performance of Ti_3AlC_2-based MAX phases with aid of machine learning. *J Adv Ceram* 2022, **11**: 1307–1318.

[53] Henkelman G, Arnaldsson A, Jónsson H. A fast and robust algorithm for Bader decomposition of charge density. *Comput Mater Sci* 2006, **36**: 354–360.

[54] Duong TT, Iitaka T, Hung PK, *et al*. The first peak splitting of the GeGe pair RDF in the correlation to network structure of GeO_2 under compression. *J Non Cryst Solids* 2017, **459**: 103–110.

[55] Dasmahapatra A, Meletis E, Kroll P. First principles modeling and simulation of Zr–Si–B–C–N ceramics: Developing hard and oxidation resistant coatings. *Acta Mater* 2017, **125**: 246–254.

[56] Stoffel RP, Wessel C, Lumey MW, *et al*. *Ab initio* thermochemistry of solid-state materials. *Angew Chem Int Ed* 2010, **49**: 5242–5266.

[57] Liang B, Yang ZH, Rao JC, *et al*. Highly dense amorphous Si_2BC_3N monoliths with excellent mechanical properties prepared by high pressure sintering. *J Am Ceram Soc* 2015, **98**: 3782–3787.

[58] Zhang PF, Jia DC, Yang ZH, *et al*. Crystallization and microstructural evolution process from the mechanically alloyed amorphous SiBCN powder to the hot-pressed nano SiC/BN(C) ceramic. *J Mater Sci* 2012, **47**: 7291–7304.

[59] Jäschke T, Jansen M. Improved durability of Si/B/N/C random inorganic networks. *J Eur Ceram Soc* 2005, **25**: 211–220.

[60] Bechelany MC, Salameh C, Viard A, *et al*. Preparation of polymer-derived Si–B–C–N monoliths by spark plasma sintering technique. *J Eur Ceram Soc* 2015, **35**: 1361–1374.

[61] Marks NA, McKenzie DR, Pailthorpe BA, *et al*. Ab initio simulations of tetrahedral amorphous carbon. *Phys Rev B* 1996, **54**: 9703–9714.

[62] Qiao JC, Wang Q, Pelletier JM, *et al*. Structural heterogeneities and mechanical behavior of amorphous alloys. *Prog Mater Sci* 2019, **104**: 250–329.

[63] Bai YL, Qi XX, He XD, *et al*. Phase stability and weak metallic bonding within ternary-layered borides CrAlB, Cr_2AlB_2, Cr_3AlB_4, and Cr_4AlB_6. *J Am Ceram Soc* 2019, **102**: 3715–3727.

[64] Jaiswal PK, Procaccia I, Rainone C, *et al*. Mechanical yield in amorphous solids: A first-order phase transition. *Phys Rev Lett* 2016, **116**: 085501.

[65] Jhi SH, Louie SG, Cohen ML, *et al*. Mechanical instability and ideal shear strength of transition metal carbides and nitrides. *Phys Rev Lett* 2001, **87**: 075503.

[66] Wang YC, Ding J, Fan Z, *et al*. Tension–compression asymmetry in amorphous silicon. *Nat Mater* 2021, **20**: 1371–1377.

[67] Cao YX, Li JD, Kou BQ, *et al*. Structural and topological nature of plasticity in sheared granular materials. *Nat Commun* 2018, **9**: 2911.

[68] Wang JY, Zhou YC, Lin ZJ. Mechanical properties and atomistic deformation mechanism of γ-$Y_2Si_2O_7$ from first-principles investigations. *Acta Mater* 2007, **55**: 6019–6026.

[69] Li WX, Wang T. Elasticity, stability, and ideal strength of β-SiC in plane-wave-based *ab initio* calculations. *Phys Rev B* 1999, **59**: 3993–4001.

[70] Li YY, Xiao W. First principles study of the C/Si ratio effect on the ideal tensile strength of β-SiC. *Comput Mater Sci* 2015, **110**: 215–220.

[71] Ogata S, Hirosaki N, Kocer C, *et al*. An *ab initio* study of the ideal tensile and shear strength of single-crystal β-Si_3N_4. *J Mater Res* 2003, **18**: 1168–1172.

[72] Wang JY, Yang ZH, Duan XM, *et al*. Microstructure and mechanical properties of SiC_f/SiBCN ceramic matrix composites. *J Adv Ceram* 2015, **4**: 31–38.

[73] Song CK, Liu YS, Ye F, *et al*. Enhanced mechanical

property and tunable dielectric property of SiC_f/SiC–SiBCN composites by CVI combined with PIP. *J Adv Ceram* 2021, **10**: 758–767.

[74] Cook J, Gordon JE, Evans CC, *et al*. A mechanism for the control of crack propagation in all-brittle systems. *P Roy Soc A-Math Phy* 1964, **282**: 508–520.

[75] Pompidou S, Lamon J. Analysis of crack deviation in ceramic matrix composites and multilayers based on the Cook and Gordon mechanism. *Compos Sci Technol* 2007, **67**: 2052–2060.

[76] Ding Q, Ni DW, Ni N, *et al*. Thermal damage and microstructure evolution mechanisms of C_f/SiBCN composites during plasma ablation. *Corros Sci* 2020, **169**: 108621.

[77] Luan XG, Xu XM, Wang L, *et al*. Long-term oxidation behavior of C/SiC–SiBCN composites in wet oxygen environment. *J Eur Ceram Soc* 2021, **41**: 1132–1141.

[78] Buet E, Sauder C, Sornin D, *et al*. Influence of surface fibre properties and textural organization of a pyrocarbon interphase on the interfacial shear stress of SiC/SiC minicomposites reinforced with Hi-Nicalon S and Tyranno SA3 fibres. *J Eur Ceram Soc* 2014, **34**: 179–188.

[79] Ding Q, Ni DW, Wang Z, *et al*. Mechanical properties and microstructure evolution of 3D C_f/SiBCN composites at elevated temperatures. *J Am Ceram Soc* 2018, **101**: 4699–4707.

[80] Xin QF. Durability and reliability in diesel engine system design. In: *Diesel Engine System Design*. Xin QF, Ed. Amsterdam, the Netherlands: Woodhead Publishing, 2013: 113–202.

[81] Aksel C, Warren PD. Thermal shock parameters [*R*, *R'''* and *R''''*] of magnesia–spinel composites. *J Eur Ceram Soc* 2003, **23**: 301–308.